IEEE Transactions on Medical Imaging

An Automated Quantification Method of Intracerebral Aneurysm Wall Enhancement Based on Surface Adaptation Algorithm

Journal:	*IEEE Transactions on Medical Imaging*
Manuscript ID	TMI-2024-3199
Manuscript Type:	Regular Paper
Date Submitted by the Author:	09-Dec-2024
Complete List of Authors:	Zhang, Junyi; Suzhou University of Science and Technology Geng, Chen; Chinese Academy of Sciences Suzhou Institute of Biomedical Engineering and Technology Lu, Yucheng; Huashan Hospital Fudan University Department of Radiology; Fudan University Xue, Peiyang; Xuzhou Medical University Bai, Dunhui; Xuzhou Medical University Dai, Bin; Chinese Academy of Sciences Suzhou Institute of Biomedical Engineering and Technology zhou, zhiyong; Chinese Academy of Sciences Suzhou Institute of Biomedical Engineering and Technology Li, Yuxin; Huashan Hospital Fudan University Department of Radiology; Fudan University Dai, Yakang; Chinese Academy of Sciences Suzhou Institute of Biomedical Engineering and Technology
Keywords:	Computational geometry < General methodology, Quantification and estimation < General methodology, Angiographic imaging < Imaging modalities, Magnetic resonance imaging (MRI) < Imaging modalities, Brain < Object of interest, Vessels < Object of interest

IEEE TRANSACTIONS ON MEDICAL IMAGING, VOL. xx, NO. X, NOVEMBER 2024

An Automated Quantification Method of Intracerebral Aneurysm Wall Enhancement Based on Surface Adaptation Algorithm

Junyi Zhang, Chen Geng, Yucheng Lu, Peiyang Xue, Dunhui Bai, Bin Dai, Zhiyong Zhou, Yuxin Li and Yakang Dai

***Abstract*—Aneurysm wall enhancement (AWE) serves as a critical biomarker for the instability of cerebral aneurysms. Quantitative assessment of AWE is imperative for the risk stratification of unruptured intracranial aneurysms (UIAs). Despite the clinical relevance, current methodologies for AWE analysis are labor-intensive and require significant manual intervention, thereby limiting their practical utility in a clinical setting. This study introduces an automated, end-to-end quantification approach for AWE, leveraging time-of-flight magnetic resonance angiography (TOF-MRA) and high-resolution vessel wall imaging (HR-VWI). Our method encompasses a surface iteration algorithm and aneurysm wall separation algorithm, facilitating voxel-level quantification and visualization of aneurysm walls through graph morphology-based transformation of the surface mesh, with minimal input in the form of rough annotations. This approach enables the efficient and automated computation of various AWE metrics with a significantly reduced time investment. Our experimental validation across 90 aneurysm cases demonstrates a high degree of concordance (ICC = 0.923, 95% CI: 0.88-0.95) between our automated method and manual annotations of wall enhancement index. This novel automatic quantification method offers a robust and objective tool for clinical assessment of aneurysm risk, streamlining the diagnostic process and enhancing patient care.**

***Index Terms*—Intracerebral Aneurysm, high-resolution vessel wall imaging (HR-VWI), aneurysm enhancement, automated quantification.**

This work was supported in part by the National Science and Technology Major Project of the Ministry of Science and Technology of China No. 2023ZD0503606; in part by National Natural Science Foundation of China U23A20483, 62441114; in part by Jiangsu Key Technology Research Development Program BE2022842; in part by Suzhou Science & Technology Projects SKY2022151, SSD2023008; and in part by Shandong Natural Science Foundation ZR2022QF093. *(Junyi Zhang and Chen Geng contributed equally to this work.) (Corresponding authors: Yakang Dai; Yuxin Li.)*

Junyi Zhang is with School of Electronic & Information Engineering, Suzhou University of Science and Technology, Suzhou, China (e-mail: zjy445719111@qq.com).

Chen Geng, Bin Dai, Zhiyong Zhou and Yakang Dai are with Suzhou Institute of Biomedical Engineering and Technology, Chinese Academy of Sciences, Suzhou, China (e-mail: gengc@sibet.ac.cn; daib@sibet.ac.cn; zhouzy@sibet.ac.cn; daiyk@sibet.ac.cn).

Yucheng Lu and Yuxin Li are with Department of Radiology, Huashan Hospital, Fudan University, Shanghai, China, and also with Institute of Functional and Molecular Medical Imaging, Fudan University, Shanghai, China (e-mail: 359918717@qq.com; liyuxin@fudan.edu).

Peiyang Xue and Dunhui Bai are with School of Biomedical Engineering, Xuzhou Medical University, Xuzhou, China (e-mail: xpy1360446222@163.com; 1538603829@qq.com).

I. Introduction

UNRUPTURED intracranial aneurysms (UIAs) are localized, pathological dilations of cerebral artery walls [1], with a global incidence of approximately 1-7% [2]. Aneurysm rupture is the primary cause of subarachnoid hemorrhage, with a mortality rate of up to 50% [3]. Therefore, accurate assessment of UIA rupture risk is crucial for clinical decision-making and treatment.

Histopathology indicates that inflammatory responses on the arterial wall are one of the mechanisms leading to aneurysm formation and growth. High-resolution vessel wall magnetic resonance imaging (HR-VWI) has become a reliable imaging method for evaluating the morphological characteristics and rupture risk of UIAs [4, 5]. Currently, the assessment of UIA rupture risk mainly relies on aneurysm morphology characteristics and aneurysm wall enhancement (AWE) [6], which is identified by observing increased signal intensity (SI) in the aneurysm wall on post-gadolinium contrast-enhanced sequences. Numerous studies find that the AWE is significantly associated with the risk of aneurysm growth and rupture, making it an important marker for aneurysm instability. Therefore, the quantitative evaluation of AWE is of great significance for predicting the stability of UIAs [7]. As shown in Fig. 1, AWE appears as an enhanced area in HR-VWI, suggesting potential inflammatory risk at the location [8].

In recent years, quantitative research on AWE assessment made significant progress. Various indicators of the AWE measurements had been proposed, such as the enhancement ratio (ER) [9], aneurysm-to-pituitary stalk contrast ratio (CR_{Stalk}) [10], and wall enhancement index (WEI) [11] proposed by Wang et al. and Omodaka et al. These indicators assessed aneurysm risk by analyzing SI characteristics of aneurysms in HR-VWI images. A multi-center study by Roa et al. showed that these measurements had good indicative value for aneurysm instability, using a maximum aneurysm diameter > 7 mm as an instability marker [12].

However, AWE assessment still faces challenges. Due to clinical limitations, the main assessment method for AWE remains visual observation of slices by physicians, which is limited by the accuracy of subjective slice selection and black-blood image reading. Additionally, current quantitative research requires manual precise annotation of the aneurysm

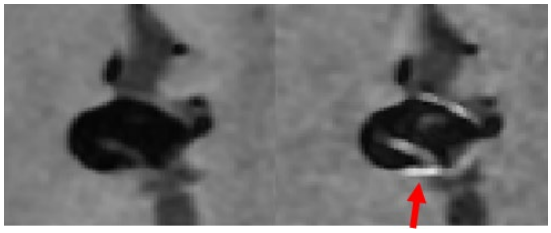

Fig. 1. Pre-contrast and post-contrast sequences. The arrow indicates a typical aneurysm wall enhancement (AWE).

wall, which is very time-consuming, so automated aneurysm wall quantification methods are urgently needed. Existing research on automated AWE quantification is limited. Raghuram et al. [13] proposed a semi-automatic quantification method based on manual fine annotation of the aneurysm wall. Veeturi et al. [14] and Fu et al. [15] obtained the outer surface of the aneurysm wall based on the artery segmentation from TOF-MRA image, then segmented the aneurysm neck manually to achieve the quantification and visualization. All of these studies use surface normal vector radial sampling to achieve SI mapping to the aneurysm wall surface but have low levels of automation, requiring intervention of professionally skilled physicians in the intermediate process, making it difficult to support large-scale clinical analysis.

To address these issues, in this study, we proposed an end-to end automated algorithm for cerebral aneurysm wall enhancement quantification which integrated TOF-MRA and HR-VWI sequences. Through point-to-point SI mapping of the inner surface of the aneurysm wall, the method could automatically calculate measurements such as the wall enhancement index (WEI), and the consistency of this method was compared with manual results.

II. Methodology

The overall method flow of this study is shown in Fig. 2. To achieve automated accurate quantification of aneurysm wall enhancement, after obtaining MR image sequences and annotations of aneurysms, we first performed image preprocessing and joint registration of TOF-MRA image, T1-weighted image (T1), and post-gadolinium contrast-enhanced T1-weighted images (T1+C). Then, using a black blood segmentation algorithm, we extracted black blood lumen masks under T1 and T1+C sequences. Subsequently, we used an adaptive algorithm to extract the aneurysm wall surface and integrated it with the black blood mask for 3D aneurysm reconstruction. Quantitative measurements were obtained through surface SI mapping. After obtaining quantification results, we compared the WEI reference points obtained by our automatic algorithm with manually selected ones, and performed correlation statistics to verify the effectiveness of the method.

A. Image Acquisition and Processing

The ethics board of our institution comprehensively reviewed and approved the protocol of this retrospective study. The informed consents were waived since all of TOF-MRA images were acquired from routine clinical work.

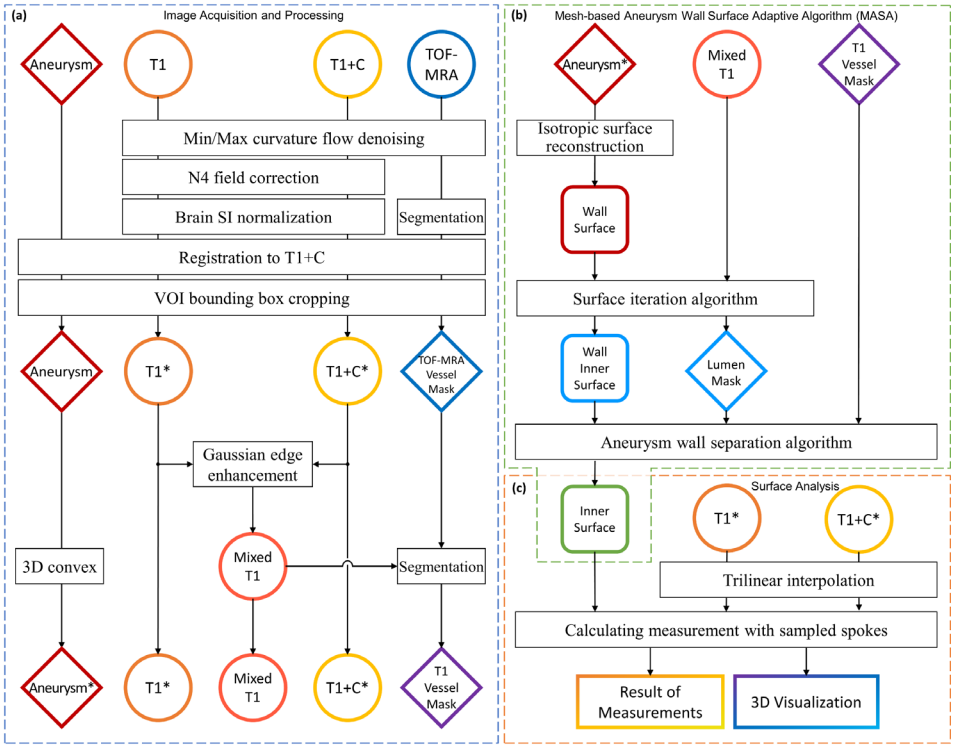

Fig. 2. Overall method flow of this study. Circles represent 3D images, diamonds represent binary images, and rounded rectangles represent 3D mesh surfaces. (a) Image acquisition and processing (b) Aneurysm wall surface adaptive algorithm (c) Surface analysis. *: Processed image data

For each aneurysm case, our method took TOF-MRA, T1, and T1+C sequences in DICOM file format as input, along with a coarse aneurysm annotation based on any of these three sequences. In this article, all coarse aneurysm annotations came from manual annotations by physicians, and we calculated 3D convex hulls as the input annotation masks. All 3D image sequences underwent min/max curvature flow denoising [16] and N4 bias field correction [17] preprocessing steps, and multi-sequence registration was performed using the SyN (Symmetric Image Normalization) method [18] to register TOF-MRA image, T1 image, and coarse aneurysm annotation to the T1+C space. Then, using the annotation, we cropped the volume of interest (VOI) bounding box from the registered TOF-MRA, T1, and T1+C sequences. Based on the WEI calculation method proposed by Omodaka [11], we proposed an improved SI calculation method that uses the peak SI of the white matter portion in the SI histogram (appearing as the maximum peak above the overall average SI) for normalization to eliminate overall SI differences between sequences. Our method ensured minimal differences in SI for non-enhanced parts between T1 and T1+C sequences, thereby guaranteeing the accuracy and consistency of SI quantification.

To obtain the complete aneurysm wall surface and separate the aneurysm lumen from the normal arterial lumen, a mask of the cerebral arterial lumen was required. We used a two-step segmentation strategy: first, we segmented the TOF-MRA sequence, obtaining an artery mask after skull stripping, high SI voxel threshold segmentation, and connected component filtering operations, sequentially. Then, through morphological dilation of the white blood mask, we obtained a candidate region for black blood segmentation. Next, we performed Gaussian filtering edge enhancement on the registered black blood sequence images I_{T1}, $I_{\mathrm{T1+C}}$ to enhance the vessel wall portion, mixing the black blood images to obtain I_{Mixed}. After masking I_{Mixed} with the candidate region for black blood segmentation, we performed threshold segmentation of low SI voxels to obtain the black blood vessel lumen mask I_{VL}. The specific formulas for this step are as equation (1-3), where I represents the 3D image matrix, and $\star$ represents the convolution operator. Equation (1) defines the continuous function of 3D Gaussian filtering, equation (2) defines the edge enhancement function, and equation (3) is the calculation formula for I_{Mixed}.

$$G(x,y,z)=\frac{1}{(2\pi)^{3/2}\sigma^{3}}\exp\left(-\frac{x^{2}+y^{2}+z^{2}}{2\sigma^{2}}\right) \quad (1)$$

$$F(I)=I+\max(0,I-G\star I) \quad (2)$$

$$I_{\mathrm{Mixed}}=F(I_{\mathrm{T1}})+F(I_{\mathrm{T1+C}}) \quad (3)$$

B. Mesh-based Aneurysm Wall Surface Adaptation Algorithm (MASA)

To obtain accurate aneurysm wall quantification results, precise boundary divisions between the aneurysm lumen and aneurysm wall were required for subsequent SI mapping. In this study, we proposed a Mesh-based Aneurysm wall Surface Adaptation Algorithm (MASA). By performing an iterative morphing process on the surface to make it fit as close as possible to the low SI region boundary in the T1 sequence, an accurate aneurysm wall inner surface was obtained.

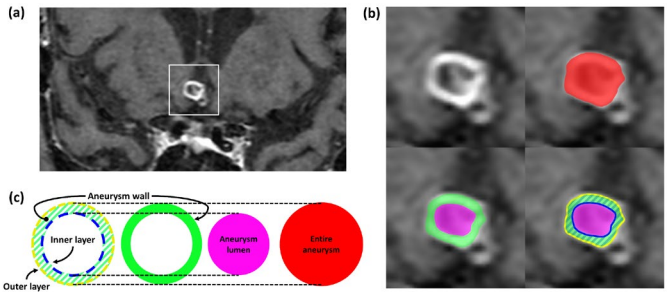

Fig. 3. Schematic diagram of aneurysm structure. (a) A clearly enhanced anterior communicating artery bifurcation aneurysm on the axial plane (b) The aneurysm wall (green), aneurysm lumen (pink), aneurysm wall inner layer (blue), and aneurysm wall outer layer (yellow) of this aneurysm (red) (c) Relationship diagram of the complete aneurysm, aneurysm wall, aneurysm lumen, aneurysm wall inner layer, and aneurysm wall outer layer. The inner and the outer layers of aneurysm walls are conceptual surfaces that separate the aneurysm lumen, aneurysm wall, and external tissues, with no physical thickness.

1) Isotropic Surface Reconstruction

After calculating the 3D convex hull of the input annotation and registering it to the T1+C sequence, we used the marching cubes algorithm [19] for 3D surface reconstruction of the annotation and used Taubin-constrained Laplacian smoothing to smooth the surface. Due to the imaging characteristics of MR scans, the voxel spacing of 3D images was anisotropic and images were relatively low resolution. We calculated the distance from the center of each voxel to the 3D surface and used this to select the collection of voxels closest to the surface, which we used to construct a smoother three-dimensional surface $\mathcal{S}$.

2) Surface Iteration Algorithm

As shown in Fig. 3, the aneurysm wall inner layer is the interface between the aneurysm lumen and the aneurysm vessel wall. In HR-VWI black blood sequences, the aneurysm lumen where blood flows appear as low SI, while the aneurysm wall appears as high SI. The inner layer of aneurysm wall was usually at the boundary between high and low SI. However, due to limitations in imaging, it is difficult to extract the aneurysm wall inner layer surface using simple edge detection. With the assumption that aneurysms are continuous smooth 3D volumes, we proposed a surface iteration algorithm of 3D meshes, which implemented adaptive extraction and 3D reconstruction of the aneurysm wall inner layer surface by introducing neighborhood smoothing as a constraint on surface curvature.

To perform smoothing and morphological operations on the 3D surface, we adopted a graph morphology method [20] using vertex neighborhood calculation. A triangular mesh could be regarded as an undirected graph composed of mesh vertices and edges. Supposed the three-dimensional mesh undirected graph of the reconstructed surface $\mathcal{S}$ was $\mathcal{G}=(\mathcal{V},\mathcal{E})$, with N vertices in total. $\mathcal{V}=\{v_1,\cdots,v_N\}$ was the vertex set of graph $\mathcal{G}$, and $\mathcal{E}$ was the edge set of graph $\mathcal{G}$. As shown in Fig. 4, for any vertex

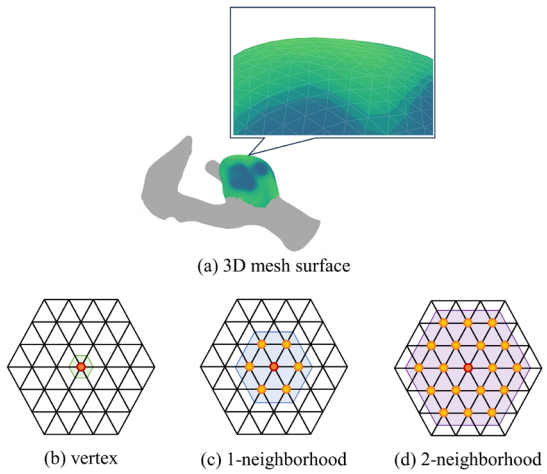

Fig. 4. Schematic diagram of neighborhood vertex sets in a 3D mesh model. (a) 3D mesh reconstruction of an aneurysm (b) A vertex on the surface (c) 1-neighborhood vertex set of that vertex (d) 2-neighborhood vertex set of that vertex.

v in the undirected graph $\mathcal{G}$, let the set of vertices that could be reached from vertex v with a minimum number of edges, which was less than or equal to k, be the k-neighborhood vertex set $\mathcal{N}_k(v)$. The 1-neighborhood vertex set $\mathcal{N}_1(v)$ and k-neighborhood vertex set $\mathcal{N}_k(v)$ $(k>1)$ could be derived recursively by equations (4) and (5).

$$\mathcal{N}_1(v)=\left\{w\in\mathcal{V}\middle|(v,w)\in\mathcal{E}\right\}\cup\{v\} \tag{4}$$

$$\mathcal{N}_k(v)=\bigcup_{u\in\mathcal{N}_{k-1}(v)}\left\{w\in\mathcal{V}\middle|(u,w)\in\mathcal{E}\right\} \tag{5}$$

$$[\boldsymbol{Q}_k]_{v,u}=\begin{cases}\dfrac{m(u)}{\sum_{w\in\mathcal{N}_k(v)}m(w)}, & \text{if } u\in\mathcal{N}_k(v);\\ 0, & \text{if } u\notin\mathcal{N}_k(v).\end{cases} \tag{6}$$

Equation (6) defines the k-neighborhood average matrix $\boldsymbol{Q}_k$, where $m(\cdot)$ represents the vertex weight, usually using the Voronoi area of the vertex as the weight value [24].

Ideally, the aneurysm wall inner layer surface was at the boundary between high and low SI, as shown in Fig. 5. The SI changed on its inner layer surface was relatively obvious, so we could use the maximum value of the derivative as the ideal boundary point for surface iteration optimization. Based on this idea, we designed iteration algorithm as follows:

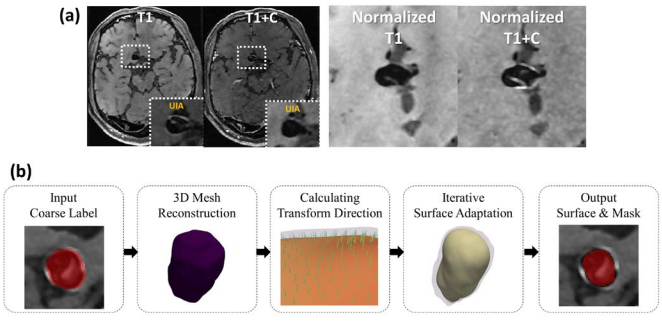

Fig. 5. (a) Schematic diagram of an aneurysm in a black blood image (b) Flow chart of the surface iteration algorithm.

Step 1: Perform trilinear interpolation on the edge-enhanced black blood image I_{Mixed} to obtain the interpolated image function $\hat{I}(\boldsymbol{x})$.

Step 2: Calculate the unit normal vector for each vertex. Let the coordinate matrix of all vertices be $\boldsymbol{X}=[\boldsymbol{x}_1,\cdots,\boldsymbol{x}_N]^\top$. Calculate the unit normal vector matrix $\boldsymbol{N}=[\boldsymbol{n}_1,\cdots,\boldsymbol{n}_N]^\top$ of all vertices on the surface.

Step 3: Calculate the transform direction of each vertex. This direction is obtained by mixing the normal vector after neighborhood averaging and the direction of the centroid ray. The unit evolution direction matrix $\boldsymbol{N}^*=[\boldsymbol{n}_1^*,\cdots,\boldsymbol{n}_N^*]^\top$ of all vertices is calculated by equations (7)-(8). Here, $\bar{\boldsymbol{x}}$ represents the centroid of the volume enclosed by the three-dimensional surface. The parameter λ adjusts the mixing ratio of the normal vector and the central ray direction. In this study, we chose $\lambda=1$.

$$\tilde{\boldsymbol{n}}_i^*=\frac{\sum_{w\in\mathcal{N}_k(i)}m(w)\boldsymbol{n}_w}{\left\|\sum_{w\in\mathcal{N}_k(i)}m(w)\boldsymbol{n}_w\right\|}+\lambda\frac{\boldsymbol{x}_i-\bar{\boldsymbol{x}}}{\left\|\boldsymbol{x}_i-\bar{\boldsymbol{x}}\right\|} \tag{7}$$

$$\boldsymbol{n}_i^*=\frac{\tilde{\boldsymbol{n}}_i^*}{\left\|\tilde{\boldsymbol{n}}_i^*\right\|} \tag{8}$$

Step 4: Calculate the directional derivative along the evolution direction of each vertex, and calculate the maximum value of the derivative within a certain range T near the vertex as the target position of each vertex after evolution. Obtain the target offset t_i^* of vertex i by equation (9), and calculate the target displacement $\boldsymbol{t}^*=[t_1^*,\cdots,t_N^*]^\top$ of all vertices. Then apply neighborhood smoothing constraints to update vertex positions, allowing the surface to deform adaptively according to assignment expression (10). The parameter $\mu\in(0,1]$ is the step size used to adjust the magnitude of iterative evolution. In this study, we chose $\mu=0.25$.

$$t_i^*=\arg\max_{t\in T}\left[\nabla\hat{I}\left(\boldsymbol{x}_i+t\cdot\boldsymbol{n}_i^*\right)\cdot\boldsymbol{n}_i^*\right] \tag{9}$$

$$\boldsymbol{X}\leftarrow\boldsymbol{X}+\mu\boldsymbol{N}^*\boldsymbol{Q}_k\boldsymbol{t}^* \tag{10}$$

Step 5: Re-mesh the surface $\mathcal{S}$ to restore the isotropy of the mesh vertices. Finally, return to **Step 2** until the surface converges.

After the above steps, we obtained the final inner surface of the aneurysm wall $\mathcal{S}_{\text{Inner}}$. However, it should be noted that since we assumed the aneurysm to be a continuous smooth three-dimensional volume, the calculated inner surface of the aneurysm wall around the aneurysm neck was not a real surface, but an approximate surface obtained by patching based on the surface around the aneurysm neck. To measure the aneurysm wall surface area and the proportion of enhanced areas more

accurately, we needed to perform an aneurysm wall separation algorithm.

3) Aneurysm Wall Separation Algorithm

After obtaining the inner surface of the aneurysm wall $\mathcal{S}_{\text{Inner}}$ through the surface iteration algorithm, we sampled the internal volume enclosed by $\mathcal{S}_{\text{Inner}}$ into the T1+C space to obtain the aneurysm lumen mask I_{AL}. In previous steps, we had already obtained the black blood vessel lumen mask I_{VL} through threshold segmentation. Due to limitations of the segmentation algorithm and differences in accuracy of the surface iteration algorithm, the aneurysm part of the mask and reconstructed surface in I_{VL} would differ from the inner surface of the aneurysm wall $\mathcal{S}_{\text{AL}}$ calculated by the surface iteration algorithm. We designed an automatic aneurysm wall-vessel wall separation algorithm to restore the vertices of the aneurysm wall part to the previously calculated inner surface position. The steps are as follows:

Step 1: Merge the vessel lumen mask I_{VL} with the aneurysm lumen mask I_{AL} by element-wise logical OR operation to obtain the merged inner lumen mask I_{Lumen}. Then use the same method to reconstruct it as a high-resolution isotropic surface $\mathcal{S}_{\text{Lumen}}$.

Step 2: Calculate the centroid $\bar{\boldsymbol{x}}$ of the volume enclosed by the inner surface of the aneurysm wall $\mathcal{S}_{\text{AL}}$, and expand the surface $\mathcal{S}_{\text{AL}}$ by a certain distance with $\bar{\boldsymbol{x}}$ as the center to obtain the expanded surface $\mathcal{S}_{\text{AL}}^{+}$.

Step 3: Calculate the part of surface $\mathcal{S}_{\text{Lumen}}$ enclosed by surface $\mathcal{S}_{\text{AL}}^{+}$ to obtain the vertex set $\mathcal{X}_{\text{Wall}}^{+}$ of this part on the three-dimensional mesh model of $\mathcal{S}_{\text{Lumen}}$ as the initial aneurysm wall separation result.

Step 4: Use graph morphology reconstruction closing operation to repair holes in $\mathcal{X}_{\text{Wall}}^{+}$, and use erosion operation to remove excess vertices selected due to the expansion of $\mathcal{S}_{\text{AL}}$ obtaining the repaired aneurysm wall vertex set $\mathcal{X}_{\text{Wall}}$.

Step 5: After obtaining the aneurysm wall vertex set $\mathcal{X}_{\text{Wall}}$, project rays from $\bar{\boldsymbol{x}}$ towards each vertex and record the coordinates of the point on the inner surface of the aneurysm wall $\mathcal{S}_{\text{AL}}$ closest to each vertex's position along the corresponding ray. Update these vertices to the hit coordinates. After completion of the calculation, we finally obtained the complete blood vessel inner surface $\mathcal{S}_{\text{Lumen}}$ and the vertex set $\mathcal{X}_{\text{Wall}}$ belonging to the aneurysm wall.

C. Surface Analysis

To calculate measurements and visualize aneurysm wall enhancement, we need to map the SI of I_{T1} and $I_{\text{T1+C}}$ to the surface $\mathcal{S}_{\text{Lumen}}$. For each vertex belonging to the aneurysm wall vertex set $\mathcal{X}_{\text{Wall}}$ on the inner surface $\mathcal{S}_{\text{Lumen}}$, we calculated its normal vector and created a line segment of fixed length extending outward from the vertex. Each line segment was sampled on the trilinear-interpolated $\hat{I}_{\text{T1}}$ and $\hat{I}_{\text{T1+C}}$. In the preprocessing stage, the T1 image and T1+C image were normalized according to the average signal density SI of the brain white matter around the aneurysm. We selected the maximum value sampled on each spoke as the sampled SI value of the vertex, which could eliminate numerical deviations caused by imaging problems. In this study, we chose a spoke sampling range of 0-1.2 mm outward along the vertex normal vector. Within this range, most surface vertices can be mapped to ideal SI values. The surface SI mapping results completed using this method are shown in Fig. 6.

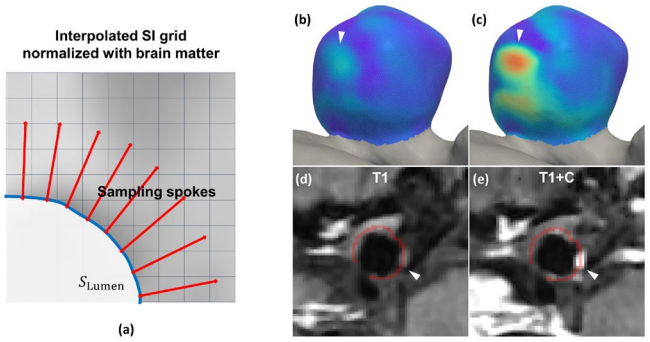

Fig. 6. Schematic diagram of surface SI mapping values. (a) Mapping method diagram. Each point on the surface samples the maximum value on the sampling line segment (red) as the mapped SI of that vertex. (b) T1 sequence mapping (c) T1+C sequence mapping (d) Locations of T1 sequence mapping points in the slice (e) Locations of T1+C sequence mapping points in the slice. The white arrows point to the same location of vessel wall enhancement.

D. Evaluation Details

To verify the effectiveness of our method, we compared the automatically calculated wall enhancement index (WEI) indicator with manual annotations by physicians to verify consistency with manual methods. WEI is an indicator for measuring aneurysm instability and widely considered as an independent factor for assessing aneurysm risk [11]. The calculation formula for the WEI of a single aneurysm is shown in equation (11):

$$\text{WEI} = \frac{\text{SI}_{\text{wall T1+C}}/\text{SI}_{\text{brain T1+C}} - \text{SI}_{\text{wall T1}}/\text{SI}_{\text{brain T1}}}{\text{SI}_{\text{wall T1}}/\text{SI}_{\text{brain T1}}} \tag{11}$$

where $\text{SI}_{\text{wall T1+C}}$ and $\text{SI}_{\text{wall T1}}$ are the highest SI values on the aneurysm wall in their respective sequences, whereas $\text{SI}_{\text{brain T1+C}}$ and $\text{SI}_{\text{brain T1}}$ are the mean SI values of brain white matter in the image around the aneurysm.

For manual annotation, physicians referred to the registered TOF-MRA three-dimensional volume reconstruction view to confirm the morphology of the aneurysm and the approximate range of the aneurysm wall. Then, following the method in [11], they selected several points with the highest SI on the aneurysm wall in the original T1 and T1+C sequences as candidate coordinates for $\text{SI}_{\text{wall T1+C}}$ and $\text{SI}_{\text{wall T1}}$. After obtaining the list of

candidate coordinates for each sequence, they calculated the registered coordinates and the final selected maximum $SI_{wall\ T1+C}$ and $SI_{wall\ T1}$ values, and used these values to calculate the WEI for each aneurysm.

Our automatic method used equation (12) to calculate the WEI for each aneurysm and records the coordinates of the vertex with the maximum value selected. Equation (12) has the same meaning as equation (11) and is the precise calculation form after mesh surface processing. Here, SI_{T1} and SI_{T1+C} are the SI mapping values of each vertex in the T1 and T1+C sequences that have been normalized with brain white matter, respectively.

$$WEI = \frac{\max\limits_{v \in \mathcal{X}_{Wall}} SI_{T1+C}(v) - \max\limits_{w \in \mathcal{X}_{Wall}} SI_{T1}(w)}{\max\limits_{w \in \mathcal{X}_{Wall}} SI_{T1}(w)} \quad (12)$$

This study used the Python scientific computing library SciPy and the data-analyzing library pingouin for data processing and statistical analysis. The Shapiro-Wilk test was used to test the normality of the data. Non-normally distributed count data were compared between groups using the Mann-Whitney *U* test and expressed as "median [interquartile range]"; normally distributed count data were compared using the t-test and expressed as "mean ± standard deviation"; unordered categorical variables were compared using the Pearson χ^2 test and expressed as "number (percentage)". The interclass correlation coefficient (ICC) and Bland-Altman method were used to evaluate the consistency between the WEI obtained by the automatic method and manual annotation by physicians. An ICC $\geqslant$ 0.75 indicates good consistency, and a 2-sided *P*-Value < 0.05 indicates statistical significance.

III. Experiments

A. Dataset

This retrospective study used research data from Huashan Hospital Affiliated to Fudan University and was approved by the ethics committee. All MR scan data came from outpatients and inpatients between March 2016 and February 2018, and were pre-treatment TOF-MRA and HR-VWI examinations. MR acquisitions were performed on a 3.0T GE (Discovery MR750) scanner. When acquiring HR-VWI, T1-weighted images (T1) were first acquired, followed by contrast-enhanced T1-weighted images (T1+C) after intravenous injection of 0.1 mmol/kg gadodiamide (Gd-BT-DO3A, produced by Bayer Schering Pharma, Berlin, Germany) based on body weight. Table I shows the acquisition parameters for TOF-MRA and different HR-VWI sequences. After excluding treated aneurysms, ruptured aneurysms, dissecting aneurysms, and poor imaging quality data, 90 aneurysms from 83 patients were ultimately used as experimental data.

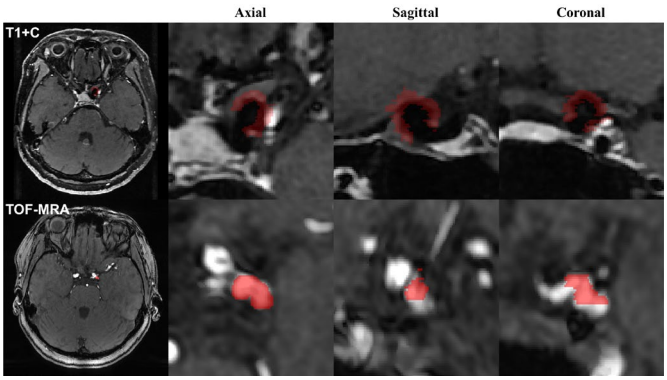

Fig. 7. Different source annotations of a sidewall aneurysm in the ophthalmic segment of the left internal carotid artery. The figure shows black blood aneurysm wall (top) and white blood aneurysm annotations (bottom). Any combination can be used as input annotation. From left to right: axial, sagittal, and coronal views.

The method proposed in this study can accept various aneurysm annotations as input, including coarse aneurysm or surface annotations on T1, T1+C, or TOF-MRA image. These annotations do not need to be particularly precise. In this study, we used two different sources of manual annotations as original aneurysm annotations for automatic quantification calculations to test the performance of the aneurysm wall adaptive algorithm. These included whole aneurysm annotations completed by a junior physician on TOF-MRA sequences (15 aneurysms) and aneurysm wall annotations completed on T1+C sequences (75 aneurysms). All annotations were completed using the ITK-SNAP annotation software. Fig. 7 shows an example of a sidewall aneurysm in the ophthalmic segment of the left internal carotid artery.

B. Results

1) Correlation Assessment of Manual Measurement

A total of 90 aneurysms (including 6 cases of multiple aneurysms) were included in the experimental calculations. The average patient age was 57.10 ± 12.06 years, with males accounting for 44.6% (44 individuals). The aneurysms comprised 55 bifurcation aneurysms (50 patients) and 35 sidewall aneurysms (33 patients). There were no significant differences in the basic demographic characteristics of the dataset.

Statistical results showed good consistency between the automated method and the manual method in calculating the Wall Enhancement Index (WEI) (ICC = 0.923, 95% CI: 0.88-0.95). The consistency in selecting the maximum SI value for

TABLE I
IMAGE ACQUISITION PARAMETERS

Sequence Name	Coil Channels	Repetition Time	Echo Time	Bandwidth	Acquisition Matrix	Field of View	Slice Thickness
3D TOF-MRA	32	25ms	5.7ms	20.83kHz	320×256	22×19.4cm²	1.2mm
T1-weighted HR-VWI*	32	600ms	13.7ms	62.5kHz	388×288	20×20cm²	1.0mm

*T1-weighted 3D CUBE fast spin-echo sequence

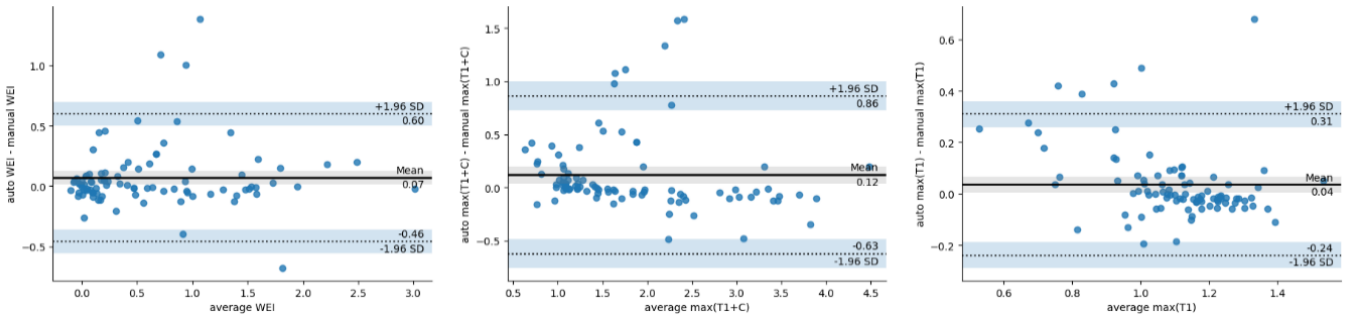

Fig. 8. Bland-Altman plots for WEI, maximum SI values of T1+C, and maximum SI values of T1

T1+C was good (ICC = 0.912, 95% CI: 0.87-0.94), whereas the consistency in selecting the maximum SI value for T1 was moderate (ICC = 0.723, 95% CI: 0.61-0.81). The Bland-Altman plot also confirmed good agreement between the automated method and manual measurements (Fig. 8).

Table II shows the basic characteristics of aneurysms grouped by size. There were no significant differences in basic demographic characteristics between aneurysms with a maximum diameter ≤ 7 mm (47 cases) and those with a maximum diameter > 7 mm (43 cases). According to the literature [12, 22], a maximum diameter > 7 mm is an important indicator of aneurysm instability. After grouping aneurysms by size, there were significant differences in WEI between groups. Our statistical results showed that the distribution of WEI values from automated measurements and manual measurements differed significantly, consistent with this conclusion. The results from the automated method were close to those from manual measurements, with minimal errors.

2) AWE Visualization Results and Aneurysm Wall SI Distribution

The automated method proposed in this paper offers a greater advantage in the quantitative analysis of all vertices on the three-dimensional surface. To demonstrate the effectiveness of our proposed method, we selected several typical aneurysms of different sizes and with or without AWE for visualization, as shown in Fig. 9. Columns 1-3 show the axial, coronal, and sagittal planes around each aneurysm in the T1+C sequence, with the contours of the surface iteration algorithm results marked in red. Columns 4-7 present the 3D visualization, intuitively displaying the 3D structure of blood vessels around the aneurysm and the SI mapping values of the aneurysm wall in T1 and T1+C sequences (columns 5 and 6), as well as the visualization of WEI mapping values reflecting the degree of AWE (column 4). The mapping value $\mathrm{AWE}_{\mathrm{WEI}}$ at vertex v is calculated using equation (13), derived from equation (12).

$$\mathrm{AWE}_{\mathrm{WEI}}(v) = \frac{\mathrm{SI}_{\mathrm{T1+C}}(v) - \max\limits_{w \in \mathcal{X}_{\mathrm{Wall}}} \mathrm{SI}_{\mathrm{T1}}(w)}{\max\limits_{w \in \mathcal{X}_{\mathrm{Wall}}} \mathrm{SI}_{\mathrm{T1}}(w)} \tag{13}$$

The maximum value of among all vertices on the surface is the WEI value for that aneurysm. Columns 7-8 show SI distribution plots, displaying the relationship between SI mapping values on the aneurysm wall surface in T1 and T1+C sequences, presented as histograms (column 7) and scatter plots (column 8).

Fig. 9 lists 4 aneurysms with observed AWE and 3 aneurysms without observed AWE. In columns 1-3 of each case, we can observe that the surface iteration algorithm results are consistent with the actual aneurysm wall inner surface in the images. Comparing the visualization results in columns 4-6, we find that the AWE group typically has a higher degree of enhancement and higher SI mapping values in the T1+C sequence. The 3D visualization results intuitively reflect the enhanced areas of the aneurysm, providing reliable assistance for clinicians in determining AWE and the degree of enhancement.

TABLE II
STATISTICAL CHARACTERISTICS GROUPED BY ANEURYSM SIZE

	Radius≤7mm N=47	**Radius>7mm N=43**	***t*/*U*/χ^2**	***P***
Age (Years)	56.62±12.25	57.56 ±11.97	-0.368	0.713
Gender				
Male	21 (44.68)	19 (44.19)	0.027	0.869
Female	26 (55.32)	24 (55.81)		
AWE				
w/ AWE	30 (63.83)	7 (16.28)	19.054	<0.001*
w/o AWE	17 (36.17)	36 (83.72)		
WEI				
Automatic	0.118 [0.012-0.417]	0.929 [0.456-1.516]	346.0	<0.001*
Manual	0.148 [0.013-0.289]	0.917 [0.351-1.506]	388.0	<0.001*
Absolute Error	0.080 [0.036-0.132]	0.055 [0.022-0.183]	1065.0	0.663

Normally distributed continuous variables, mean ± standard deviation; non-normally distributed type variables, median [interquartile range]; categorical variables, numbers (percentages).

*: $P < 0.05$, significant

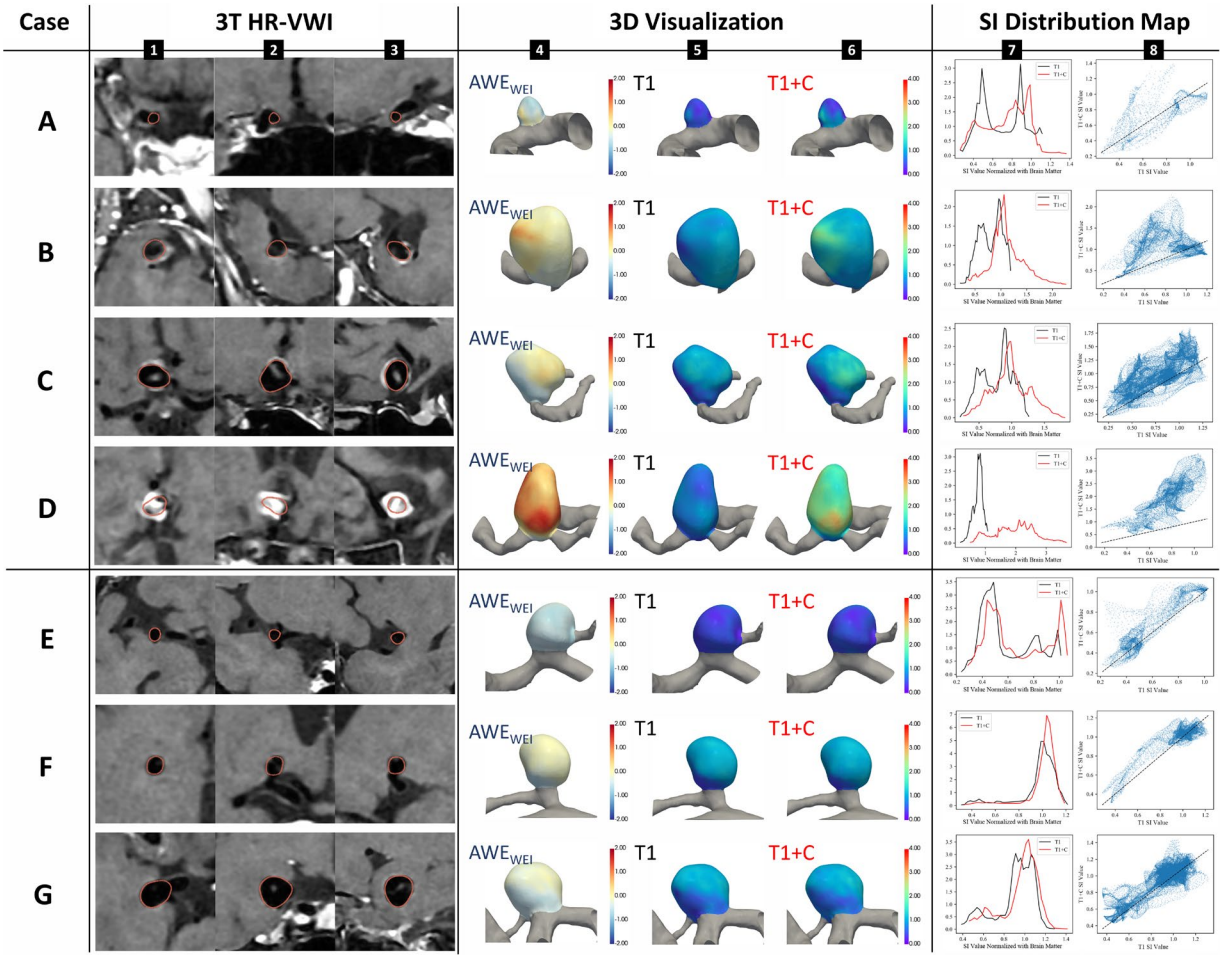

Fig. 9. Quantification and visualization results. Column 1-3: axial, coronal, and sagittal planes of 3T HR-VWI enhancement sequences, and outlines of the results of the surface iterative algorithm (in red); column 4-6: heatmap of the AWE$_{WEI}$ values, heatmap of the normalized SI mapping of cerebral white matter in the T1 sequence, heatmap of cerebral white matter normalized SI mapping in the T1+C sequence; column 7-8: histograms of the SI mapping values in T1 vs. T1+C sequences, and scatterplots of the distributions of SI. Row A-D: aneurysms with AWE observed, with a dashed line of slope 1; row E-G: aneurysms with no AWE observed. A: Right internal carotid artery ophthalmic segment sidewall aneurysm, maximum diameter 3.61mm, manually measured WEI -0.05, automatically measured WEI 0.25; B: Right middle cerebral artery M1-2 segment bifurcation aneurysm, maximum diameter 7.78mm, manually measured WEI 0.95, automatically measured WEI 0.83; C: Anterior communicating artery bifurcation aneurysm, maximum diameter 13.29mm, manually measured WEI 0.41, automatically measured WEI 0.42; D: Left anterior cerebral artery A2 segment sidewall aneurysm, maximum diameter 8.02mm, manually measured WEI 2.13, automatically measured WEI 2.31. E: Anterior communicating artery bifurcation aneurysm, maximum diameter 3.08mm, manually measured WEI 0.12, automatically measured WEI 0.07; F: Right anterior cerebral artery A1 segment sidewall aneurysm, maximum diameter 6.56mm, manually measured WEI 0.00, automatically measured WEI 0.00; G: Right posterior communicating artery bifurcation aneurysm, maximum diameter 12.20mm, manually measured WEI 0.07, automatically measured WEI 0.10.

By observing the voxel density distribution plots, we can see that the T1 and T1+C histogram curves for the non-AWE group are relatively overlapping, whereas the T1+C curve for the AWE group typically has a wider distribution and a higher upper limit. The SI scatter plots reflect the relationship between T1 (x-axis) and T1+C (y-axis) SI at each corresponding point on the aneurysm wall. In the examples, most points in the SI scatter plots tend to fall above the $y = x$ line, and in the non-AWE group with no apparent enhancement, the scatter points are concentrated around the $y = x$ line. We calculated the slope $k = y / x$ from the origin to each point in the SI scatter plot, where each slope represents the ratio of enhanced to non-enhanced SI normalized to brain white matter at the corresponding vertex position on the aneurysm wall. We then sorted the slopes k corresponding to all vertices on the surface of each individual aneurysm to obtain percentile values (2.5th, 25th, 50th, 75th, and 97.5th percentiles). The slope distributions for the non-AWE and AWE groups were statistically analyzed, as shown in Table III, with the corresponding group box plots shown in Fig. 10.

IV. Discussion

This study proposed an automated quantification algorithm for cerebral aneurysm wall enhancement based on TOF-MRA and HR-VWI sequences, utilizing three-dimensional meshes to describe surfaces and implementing an adaptive algorithm for the aneurysm wall surface. The proposed adaptive method for the aneurysm wall surface focuses on extracting the inner layer of the wall. Since the shape of the inner layer is typically more regular and has distinct SI characteristics in HR-VWI, the

TABLE III
DISTRIBUTION CHARACTERISTICS OF THE SLOPES OF SCATTER POINTS TO THE ORIGIN

	w/o AWE N=37	w/ AWE N=53	$t/U/\chi^2$	*P*
Scatter to origin Slope *k*				
2.5th percentile	0.816 [0.772-0.861]	0.836 [0.761-0.932]	847.0	0.275
25th percentile	0.963 [0.919-0.999]	1.042 [0.948-1.127]	595.0	0.002*
50th percentile	1.044 [0.998-1.105]	1.177 [1.077-1.422]	434.0	<0.001*
75th percentile	1.174 [1.101-1.251]	1.522 [1.261-1.988]	327.0	<0.001*
97.5th percentile	1.495 [1.379-1.699]	2.543 [2.052-2.892]	290.0	<0.001*
Quartile distance of *k*	0.194 [0.157-0.281]	0.469 [0.312-0.817]	309.0	<0.001*
Percentile where *k*=1	34.57 [25.10-50.33]	16.33 [8.51-35.54]	1412.0	<0.001*

Non-normally distributed type variables, median [interquartile range].
*: $P < 0.05$, significant

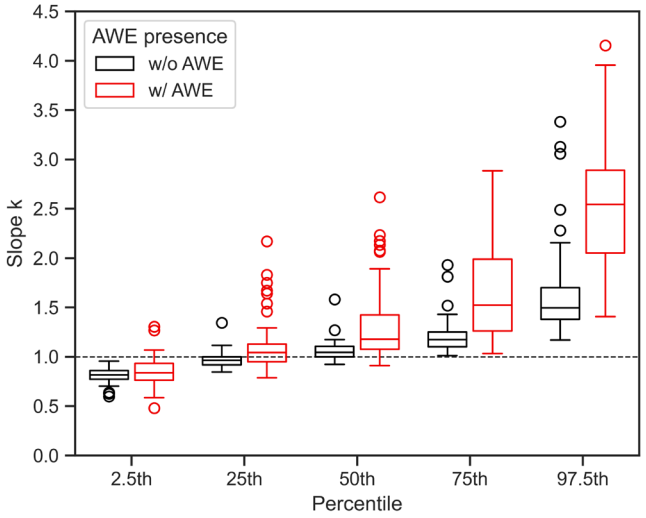

Fig. 10. Box plot of the slopes of scatter points to the origin at the [2.5th, 25th, 50th, 75th, 97.5th] percentiles in groups w/o AWE vs. w/ AWE.

extracted inner surface is more reliable. Our method also achieved point-to-point SI mapping of the inner layer surface of the aneurysm wall. Compared to traditional methods of regional averaging or maximum value selection, this approach more accurately reflects the enhancement of various parts of the aneurysm wall, providing a foundation for three-dimensional visualization and local enhancement analysis.

When studying the relationship between AWE and aneurysm wall surface SI distribution, we found that our proposed brain white matter SI value normalization strategy may be more objective and accurate compared to traditional T1 and T1+C sequence SI normalization strategies (such as sampling around the corpus callosum to obtain the average SI value of brain white matter). This was verified in the SI histogram analysis and scatter plot slope analysis (Table III, Fig. 9, Fig. 10): the non-AWE group showed small differences between T1 and T1+C (scatter points tended to distribute around the slope 1 line, with the percentile of slope 1 at 34.57 [25.10-50.33]), while the AWE group showed significantly increased SI in the T1+C sequence (scatter points tended to distribute above the slope 1 line, with the percentile of slope 1 at 16.33 [8.51-35.54]). Using the peak value of brain white matter in the SI histogram for SI normalization effectively eliminates differences in unenhanced parts between T1 and T1+C sequences, ensuring the accuracy and consistency of SI quantification. Our research also suggests the possibility of automatic AWE classification through quantitative analysis of all vertices on the three-dimensional surface. Both SI histograms and SI scatter plots intuitively demonstrate the SI change relationship between T1 and T1+C, offering significant analytical value.

In testing of 90 cases, we measured the average computation time for each major step. Preprocessing times were: N4 correction for T1 dual sequences 108.318 s, white blood segmentation 21.992 s, and multi-sequence registration 44.457 s. The main algorithm times were: brain white matter normalization-edge enhancement preprocessing 3.599 s, black blood segmentation 0.108 s, surface iteration algorithm 5.135 s, aneurysm wall separation algorithm 20.452 s, and surface analysis 0.786 s. The total preprocessing time was 174.767 s, and the total main algorithm time was 30.080 s. Compared to manual involvement in aneurysm segmentation or point annotation, our method offers certain efficiency advantages.

Additionally, this study has several limitations: (1) We co-registered TOF-MRA and T1 sequences to the T1+C sequence, which may lead to some loss of original image precision. Future studies should consider registering low-resolution images to high-resolution images (e.g., from T1 to TOF) to maximize the retention of details in high-resolution images. (2) In the T1+C sequence, high SI tissues around the aneurysm wall may affect the selection of maximum SI values. Future work could consider eliminating this influence through SI feature analysis. (3) All data in this study came from 3T HR-VWI scans, but the literature suggests that aneurysm wall imaging thickness is affected by magnetic flux magnitude [23]. The reliability of our method under different data sources requires validation with more data. In the future, we will conduct in-depth research on these issues and improve the automatic quantification method based on clinical and practical application needs.

V. CONCLUSION

This paper proposed a method for automatic quantification and three-dimensional visualization of aneurysm wall enhancement using TOF-MRA and HR-VWI images. The algorithm has relatively flexible requirements for the initial input labels and is capable of completing all calculations and visualizations without the need for manual intervention, requiring only coarse aneurysm annotations. Experimental results show that our method has good consistency with manual measurements. The three-dimensional visualization results can

reflect the degree and range of aneurysm wall enhancement, which can be used to assist the clinical diagnosis of aneurysms.

REFERENCES

[1] M. H. Vlak, A. Algra, R. Brandenburg, and G. J. Rinkel. Prevalence of unruptured intracranial aneurysms, with emphasis on sex, age, comorbidity, country, and time period: a systematic review and meta-analysis." *The Lancet Neurology* 10.7 (2011): 626-636.

[2] J. Mocco et al.; International Study of Unruptured Intracranial Aneurysms Investigators, "Aneurysm morphology and prediction of rupture: An international study of unruptured intracranial aneurysms analysis," *Neurosurgery*, vol. 82, no. 4, pp. 491–496, Apr. 1 2018.

[3] D. J. Nieuwkamp, L. E. Setz, A. Algra, F. H. Linn, N. K. de Rooij, and G. J. Rinkel, "Changes in case fatality of aneurysmal subarachnoid haemorrhage over time, according to age, sex, and region: A meta-analysis," *Lancet Neurol.*, vol. 8, no. 7, pp. 635–642, Jul. 2009.

[4] F. Li, Y. Wang, T. Hu, and Y. Wu, "Application and interpretation of vessel wall magnetic resonance imaging for intracranial atherosclerosis: A narrative review," *Ann. Transl. Med.*, vol. 10, no. 12, p. 714, Jun. 2022.

[5] B. Sui, and P. Gao, "High-resolution vessel wall magnetic resonance imaging of carotid and intracranial vessels," *Acta Radiol.*, vol. 60, no. 10, pp. 1329–1340, Oct. 2019.

[6] C. Zhu et al., "Wall enhancement of intracranial unruptured aneurysm is associated with increased rupture risk and traditional risk factors," *Eur. Radiol.*, vol. 28, no. 12, pp. 5019–5026, Dec. 2018.

[7] T. Matsushige et al., "Vessel wall imaging of evolving unruptured intracranial aneurysms," *Stroke*, vol. 50, no. 7, pp. 1891–1894, Jul. 2019.

[8] S. Nagahata et al., "Wall enhancement of the intracranial aneurysms revealed by magnetic resonance vessel wall imaging using three-dimensional turbo spin-echo sequence with motion-sensitized driven-equilibrium: A sign of ruptured aneurysm?" *Clin. Neuroradiol.*, vol. 26, no. 3, pp. 277–283, Sep. 2016.

[9] G. Wang, L. Wen, S. Lei, Q. Ran, and J. Yin. "Wall enhancement ratio and partial wall enhancement on MRI associated with the rupture of intracranial aneurysms." *Journal of NeuroInterventional Surgery* 10.6 (2018): 566-570.

[10] S. Omodaka et al., "Circumferential wall enhancement in evolving intracranial aneurysms on magnetic resonance vessel wall imaging," *J. Neurosurg.*, vol. 131, no. 4, pp. 1262–1268, Oct. 19 2018.

[11] S. Omodaka et al., "Quantitative assessment of circumferential enhancement along the wall of cerebral aneurysms using MR imaging," *AJNR Am. J. Neuroradiol.*, vol. 37, no. 7, pp. 1262–1266, Jul. 2016.

[12] J. A. Roa et al., "Objective quantification of contrast enhancement of unruptured intracranial aneurysms: A high-resolution vessel wall imaging validation study," *J. Neurosurg.*, vol. 134, no. 3, pp. 862–869, Feb. 7 2020.

[13] A. Raghuram et al. "Topographical analysis of aneurysm wall enhancement with 3-dimensional mapping." *Stroke: Vascular and Interventional Neurology* 2.4 (2022): e000309.

[14] S. S. Veeturi et al. "Aneurysm risk metrics and hemodynamics are associated with greater vessel wall enhancement in intracranial aneurysms." *Royal Society open science* 8.11 (2021): 211119.

[15] M. Fu et al. "Aneurysmal wall enhancement and hemodynamics: pixel-level correlation between spatial distribution." *Quantitative imaging in medicine and surgery* 12.7 (2022): 3692.

[16] R. Malladi, and J. A. Sethian, "Flows under min/max curvature flow and mean curvature: Applications in image processing." Computer Vision—ECCV'96: *4th European Conference on Computer Vision Cambridge*, *UK*, April 15–18, 1996 Proceedings, *Volume I* 4. Springer Berlin Heidelberg, 1996.

[17] N. J. Tustison et al., "N4ITK: Improved N3 bias correction," *IEEE Trans. Med. Imaging*, vol. 29, no. 6, pp. 1310–1320, Jun. 2010.

[18] B. B. Avants, C. L. Epstein, M. Grossman, and J. C. Gee, "Symmetric diffeomorphic image registration with cross-correlation: Evaluating automated labeling of elderly and neurodegenerative brain," *Med. Image Anal.*, vol. 12, no. 1, pp. 26–41, Feb. 2008.

[19] W. E. Lorensen, and H. E. Cline. "Marching cubes: A high resolution 3D surface construction algorithm." *Seminal graphics: pioneering efforts that shaped the field*. 1998. 347-353.

[20] H. J. A. M. Heumans, P. Nacken, A. Toet, and L. Vincent, "Graph morphology," *J. Vis. Commun. Image Represent.*, vol. 3, no. 1, pp. 24–38, 1992.

[21] A. Raghuram et al. "Semiautomated 3D mapping of aneurysmal wall enhancement with 7T-MRI." *Scientific reports* 11.1 (2021): 18344.

[22] N. Lv et al., "Wall enhancement, hemodynamics, and morphology in unruptured intracranial aneurysms with high rupture risk," *Transl. Stroke Res.*, vol. 11, no. 5, pp. 882–889, Oct. 2020.

[23] J. Feng et al., "Comparison of 7 T and 3 T vessel wall MRI for the evaluation of intracranial aneurysm wall," *Eur. Radiol.*, vol. 32, no. 4, pp. 2384–2392, Apr. 2022.

[24] M. Meyer et al., "Discrete differential-geometry operators for triangulated 2-manifolds." *Visualization and mathematics III*. Springer Berlin Heidelberg, 2003.